J Mater Sci: Mater Electron **(2026) 37:876**

A comprehensive optical band-gap investigation of GO–MWCNT reinforced CMC/PVP bionanocomposites

Ömer Bahadır Mergen[1,*] and Ertan Arda[2]

[1] *Department of Medical Imaging Techniques, Dokuz Eylul University, Izmir, Turkey*
[2] *Department of Physics, Faculty of Science, Trakya University, Edirne, Turkey*

Received: 9 December 2025
Accepted: 15 April 2026
Published online: 21 April 2026

© The Author(s), 2026

ABSTRACT

This study investigates the optical characteristics of CMC/PVP based bionanocomposites reinforced with carbon nanostructures, including graphene oxide (GO), multi-walled carbon nanotubes (MWCNTs), and their hybrid combinations. Four films, BNC0 (pristine CMC/PVP), BNC1 (GO), BNC2 (MWCNT), and BNC3 (GO/MWCNT), were fabricated via an environmentally friendly solution casting method and characterized using UV–Vis spectroscopy, FTIR, and SEM. SEM analyses revealed microscale heterogeneity arising from partial agglomeration, while the carbon fillers remained overall uniformly dispersed within the polymer matrix. FTIR confirmed functional group interactions among CMC, PVP, and the nanofillers, while UV–Vis measurements demonstrated enhanced optical absorption and a pronounced red shift in the absorption edge upon incorporation of GO and MWCNTs, particularly in the hybrid BNC3 film. The optical band-gap energy (E_g) was determined using Tauc, Absorbance Spectrum Fitting (ASF), Kubelka–Munk (K–M), and dielectric loss methods, all of which consistently indicated significant band-gap narrowing with increasing filler content due to the formation of localized states and improved charge transfer pathways. Urbach energy (E_u) calculations revealed broader band tails and increased structural disorder in the nanocomposites. Furthermore, the presence of carbon fillers markedly increased the refractive index (n), dielectric constants (ε_r, ε_i), and extinction coefficient (k), confirming improved polarization, carrier mobility, and electromagnetic loss behavior. Overall, the combined incorporation of GO and MWCNTs improves the optical absorption and dielectric properties of CMC/PVP bionanocomposites, suggesting their potential for optoelectronic and photonic applications.

Address correspondence to E-mail: bahadir.mergen@deu.edu.tr

https://doi.org/10.1007/s10854-026-17312-x

1 Introduction

The modification of polymer matrices with carbon-based nanofillers has emerged as a major research direction in the design of next generation optical and electronic materials. In particular, the integration of biopolymer/synthetic polymer blends with various nanocarbon species has opened a wide application space in nanocomposite engineering, as such hybrid systems provide significant improvements in optical response and charge transport behavior. Polymer blends are widely recognized in numerous industrial applications due to their versatile and tunable characteristics, and their technological relevance has been strengthened by the discovery of enhanced optical, electrical, structural, thermal, and mechanical properties [1]. In the context of increasing global demands for sustainability, biopolymer-based nanocomposites hold strategic importance for the development of biodegradable and environmentally benign material platforms. Accordingly, reinforcing biocompatible polymers such as CMC and PVP with carbon nanotubes (CNTs), graphene oxide (GO), or hybrid CNT/GO systems offers promising opportunities for tailoring optical band-gap engineering and dielectric performance.

Recent studies have further demonstrated that carbon-based nanofillers play a crucial role in improving interfacial interactions, dispersion behavior, and the overall physicochemical performance of polymer nanocomposites [2, 3]. In particular, hybrid nanofiller systems combining GO and CNTs have attracted increasing attention due to their complementary effects in enhancing dielectric response, optical absorption, and structural stability [4, 5]. Moreover, such hybrid systems have been reported to improve polarization mechanisms and charge transport pathways, leading to enhanced functional performance in polymer-based nanocomposites [6, 7].

Carbon-based nanostructures have constituted a core research field in optical materials science owing to their high charge carrier mobility, large surface area, exceptional thermal and electrical conductivity, and versatile functionalizability. Carbon nanotubes, in particular, have attracted considerable interest due to their remarkable optical properties and high thermal conductivity [8]. Similarly, the functional groups present on GO surfaces—such as hydroxyl, carboxyl, epoxy, and carbonyl moieties—can strengthen polymer–filler interactions and profoundly influence optical transition behavior. The non-toxic nature of GO and its ability to significantly improve polymer properties even at low concentrations make it a valuable nanofiller in modern nanocomposite design [9]. Recent reports have also highlighted that graphene-derived nanostructures and CNT-based systems significantly influence optical constants, dielectric relaxation, and interfacial polarization in polymer matrices [4, 10].

Biopolymer matrices such as carboxymethyl cellulose (CMC) and polyvinylpyrrolidone (PVP) have gained increasing attention due to their biodegradability, non-toxicity, and excellent film-forming ability. Recent advances indicate that the incorporation of carbon-based nanofillers into such matrices significantly modifies the structural, optical, and dielectric properties, making them promising candidates for advanced optoelectronic and photonic applications [11, 12]. Furthermore, emerging studies have explored the design of multifunctional polymer nanocomposites with improved stability, tunable band-gaps, and enhanced interfacial compatibility [13].

The optical band-gap (E_g) is one of the fundamental parameters governing the functional performance of semiconducting materials. As a critical parameter for photovoltaics, solar cells, lasers, and optoelectronic devices [14], the accurate determination of E_g is essential for understanding light–matter interaction, photon absorption mechanisms, and optical transition characteristics. However, each method used to estimate the band-gap has certain inherent limitations. In this context, four primary approaches are most widely employed for E_g determination in the literature: Tauc extrapolation, absorbance spectrum fitting (ASF), the Kubelka–Munk (K–M) transformation, and dielectric loss (ε_i) analysis.

The Tauc method determines the band-gap based on the energy dependence of the absorption coefficient and can be applied to both direct and indirect transitions. It has long played a central role in characterizing band-gaps in bulk and thin-film semiconductors [15]. Nevertheless, its reliance on film thickness for calculating the absorption coefficient presents a notable limitation in many thin-film studies. The ASF method, which relies directly on absorbance rather than the absorption coefficient, becomes highly advantageous when the film thickness is unknown. This feature makes ASF particularly suitable for biopolymer-based thin films and similar systems. The Kubelka–Munk transformation, especially when applied to UV–Vis diffuse reflectance (DRS) data, enables band-gap estimation without requiring thickness information and is

widely used in semiconductor analysis [16]. However, uncertainties in selecting the correct transition type may affect the reliability of the extracted E_g values. The dielectric loss (ε_i) method provides an alternative approach by evaluating near-edge electronic transitions without requiring transition-type assumptions, although ambiguities may still arise when the absorption edge is not well defined. Despite the significant progress in carbon-based polymer nanocomposites, the combined effects of GO and MWCNTs within biopolymer blends such as CMC/PVP have not been systematically investigated, particularly in terms of their influence on optical band-gap determination and dielectric behavior using multiple analytical approaches.

In this study, the influence of different carbon-based nanofillers on optical band-gap engineering in CMC/PVP (BNC0), CMC/PVP/GO (BNC1), CMC/PVP/MWCNT (BNC2), and CMC/PVP/GO/MWCNT (BNC3) bionanocomposites is comprehensively investigated. Using UV–Vis absorption and diffuse reflectance data, E_g values obtained from Tauc extrapolation, the ASF, Kubelka–Munk, and dielectric loss methods are comparatively evaluated. Additionally, the effect of film thickness on band-gap estimation is examined. A simplified and practical ASF-based approach is introduced, and Urbach energy (E_u) values are determined using both absorption coefficient and absorbance-based methods. Furthermore, the effects of GO and MWCNT incorporation on key optical parameters, including absorption coefficient (α), extinction coefficient (k), absorption edge behavior, refractive index (n), and dielectric response, are systematically analyzed. The main motivation of this work is to investigate the combined effects of GO and MWCNTs on the optical and dielectric properties of CMC/PVP-based nanocomposites, while critically comparing different band-gap determination methods.

2 Material and method

2.1 Materials

Carboxymethyl Cellulose Sodium powder (BCA-299503, Boston USA Chemistry LLC, Boston, MA, USA) and polyvinylpyrrolidone K30 (4607, Carl Roth GmbH + Co. KG, Karlsruhe, Germany) were employed to prepare the hybrid polymer matrix. The viscosity of CMC was 50–200 mPa·s (dry basis ≥ 96%), while the molecular weight of PVP was 40,000 g·mol^{-1} with a melting point of 130 °C. As carbon-based fillers, aligned multi-walled carbon nanotubes (MWCNTs, NG01AM0101) and single-layer graphene oxide (GO, NG01GO0101) supplied by Nanografi (Çankaya/Ankara 06800, Turkey) were utilized. The MWCNTs exhibited a purity greater than 96 wt%, outer diameters of 8–18 nm, inner diameters of 6 nm, lengths of 9–14 μm, and specific surface areas ranging from 30 to 300 m^2·g^{-1}. The GO possessed a purity of 99.5%, a lateral size of approximately 2 μm, and a thickness of 1 nm. Double distilled water was used as the solvent. Quartz glass substrates, transparent to UV light and measuring 2.5 × 2.5 cm^2, were employed for film deposition. All analytical-grade reagents were used without further purification.

2.2 Preparation of bionanocomposite (BNC) films

To fabricate water-soluble bionanocomposites (BNCs), an environmentally friendly solution casting technique was employed. For BNC preparation, 400 mg of CMC and 400 mg of PVP were separately dissolved in 40 mL of double distilled water under magnetic stirring at approximately 70 °C for 2 h, followed by cooling to room temperature under continuous stirring. The resulting solutions were then combined under magnetic stirring to form a homogeneous CMC/PVP host hybrid polymer solution. Subsequently, carbon fillers graphene oxide (GO) and multi-walled carbon nanotubes (MWCNTs) were incorporated into the CMC/PVP host solution in the ratios specified in Table 1. To ensure uniform dispersion of GO and MWCNTs within the CMC/PVP matrix, the mixtures were subjected to sonication for 10 min after every 6 h of stirring, and the process continued for a total of 48 h at room temperature. Homogeneous BNC solutions were thus obtained. From each solution, 0.5 mL aliquots were deposited onto 2.5 × 2.5 cm^2 quartz glass substrates-transparent to UV light-forming two films per BNC composition. The coated substrates were left to dry at room temperature for 72 h. A photograph of the resulting BNC films is presented in Fig. 1. Film thicknesses were measured using a digital micrometer with a precision of ± 1 μm, yielding values in the range of 30.0 ± 1.41 μm to 39.0 ± 1.41 μm (Table 1).

Table 1 Composition of BNC films

Bio-nanocomposites	Film thicknesses (μm)	CMC (mg)	PVP (mg)	GO (mg)	MWCNT (mg)
BNC0	30.0 ± 1.41	400	400	–	–
BNC1	33.5 ± 0.70	400	400	25	–
BNC2	35.5 ± 2.12	400	400	–	25
BNC3	39.0 ± 1.41	400	400	20	20

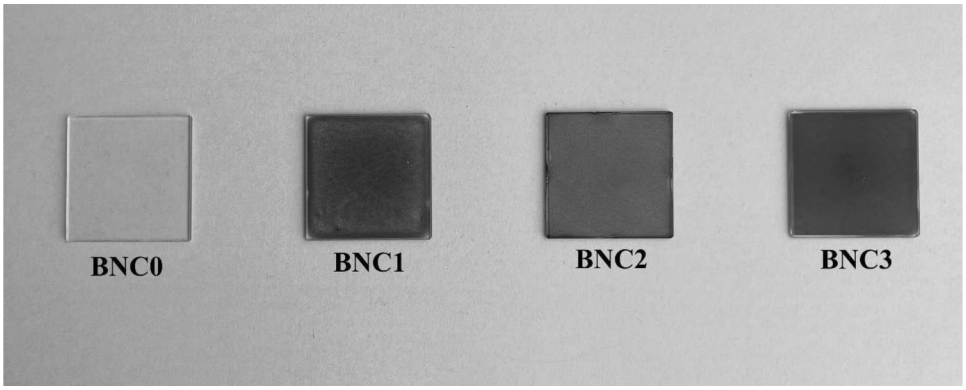

Fig. 1 Photographs of the prepared BNC films

2.3 Measurements

The optical properties of the prepared bionanocomposite films were analyzed using a UV–Vis spectrophotometer (Cary 100 Win, Agilent Technologies, Santa Clara, CA, USA) in the wavelength range of 190–900 nm. The FTIR spectra of all samples were recorded using an FTIR spectrometer (Frontier, PerkinElmer, Waltham, MA, USA) operating in the range of 4000–500 cm^{-1} to identify the characteristic functional groups and possible interactions between the polymer matrix and nanofillers. The surface morphology and dispersion of the nanostructures within the polymer matrix were examined using scanning electron microscopy (SEM; EM-30 Plus, COXEM Co., Ltd., Daejeon, South Korea).

3 Results and discussion

3.1 Scanning electron microscopy (SEM) analysis

To examine the morphological alterations induced by the incorporation of carbon fillers, scanning electron microscopy (SEM) analysis was performed on BNC1, BNC2, and BNC3 samples, as shown in Fig. 2. The micrographs reveal a random distribution of carbon fillers throughout the CMC/PVP hybrid polymer matrix. As expected, the bionanocomposite films display a notably heterogeneous morphology, reflecting the structural complexity arising from the integration of nanofillers within the polymeric backbone. Overall, the SEM images exhibit a partially agglomerated and porous microstructure, which can be attributed to the intrinsic tendency of carbon-based fillers to cluster in order to minimize their high surface energy. Nevertheless, the overall dispersion of the fillers remains relatively uniform within the matrix. This improved distribution is most likely due to the presence of hydroxyl (− OH) groups along the CMC/PVP backbone, which facilitate hydrogen bonding formation with the oxygen containing functional groups on the surface of graphene oxide (GO) [17]. Such intermolecular interactions enhance interfacial compatibility between the polymer chains and the carbonaceous fillers, thereby improving the mechanical integrity and structural cohesion of the resulting bionanocomposites. These morphological observations further support the successful incorporation and stabilization of carbon nanostructures within the polymer matrix, corroborating the homogeneous character of the prepared films at the macroscopic level.

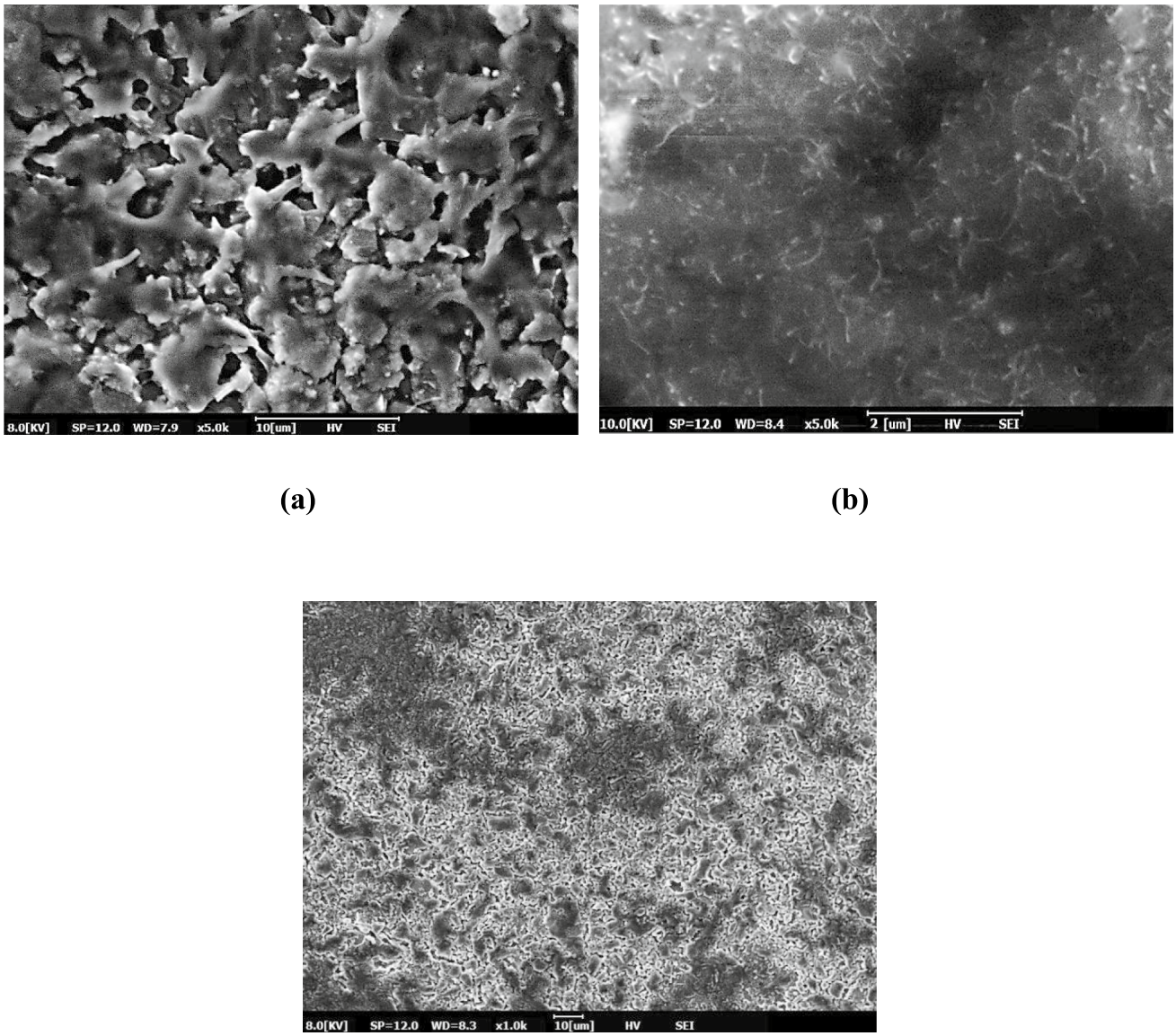

Fig. 2 SEM micrographs of the BNC films: **a** BNC1, **b** BNC2, and **c** BNC3

3.2 FTIR analysis

To investigate the functional groups and possible interactions present in the bionanocomposites (BNCs), fourier-transform infrared (FTIR) spectra were recorded, as shown in Fig. 3. The obtained spectra exhibit characteristic absorption bands at approximately 3675, 2987–2901, 1394, 990, 784, and 582 cm^{-1}. The band observed around 3675 cm^{-1} corresponds to the hydroxyl (− OH) groups of CMC, indicating the presence of hydrogen bonding interactions [18]. The bands appearing in the 2987–2901 cm^{-1} region are attributed to the C–H stretching vibrations of the aliphatic CH_2/CH_3 groups within the CMC and PVP chains. The absorption band at 1394 cm^{-1} is assigned to the symmetric stretching vibration of the carboxymethyl ($-COO^-$) group of CMC. The strong band observed near 990 cm^{-1} can be ascribed to C–O–C and C-O stretching vibrations associated with the polysaccharide backbone. The presence of these characteristic

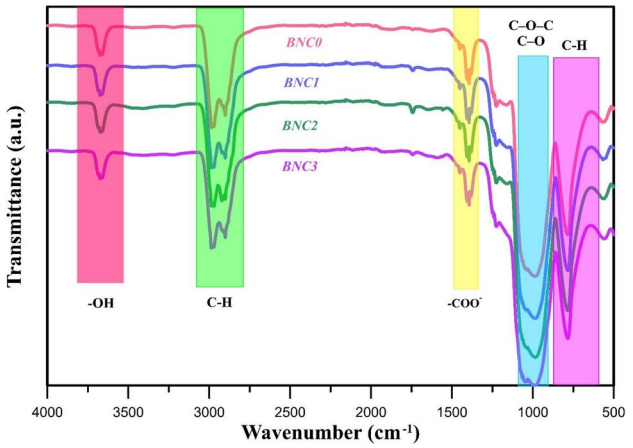

Fig. 3 FTIR spectra of the BNC films

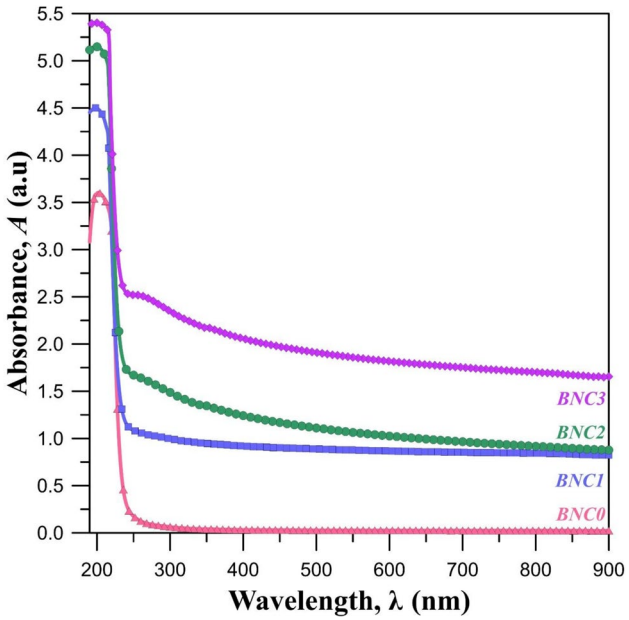

Fig. 4 The Absorbance (*A*) spectra of BNC films

functional groups confirms the miscibility of the composite components and indicates intermolecular interactions through hydrogen bonding [19]. Additionally, the bands detected at 784 and 582 cm^{-1} correspond to out-of-plane C-H bending and C–C/C-O skeletal deformation modes, respectively.

It should be noted that no significant peak shift or pronounced change in peak intensity is observed upon the incorporation of GO and MWCNTs into the polymer matrix. This behavior can be attributed to the relatively low filler content and the dominance of the polymer matrix in the FTIR response. The interactions between the nanofillers and the polymer chains are primarily governed by non-covalent mechanisms such as hydrogen bonding and weak interfacial interactions, rather than the formation of new chemical bonds. As a result, these interactions may not lead to distinct spectral shifts but can still influence the local chemical environment. In addition, possible contributions from GO functional groups may overlap with the characteristic bands of CMC and PVP, making subtle changes difficult to resolve in the spectra. Therefore, the absence of clear peak shifts does not indicate a lack of interaction but rather suggests that the interactions are weak or spectroscopically masked within the composite system.

3.3 UV–Vis analysis

The examination of optical absorption spectra is considered one of the most direct and effective methods for understanding the band structure, energy gap, and electronic transition characteristics of solid materials in both amorphous and crystalline forms [20–22]. UV–visible (UV–Vis) spectroscopy, in particular, is a powerful characterization technique widely used to evaluate the optical behavior of polymeric materials and nanocomposites [23]. This technique enables the determination of fundamental parameters, such as the energy band-gap, absorption coefficient, optical conductivity, and extinction coefficient by analyzing the light absorption tendencies of materials [24, 25]. Moreover, the position and shape of the optical absorption edge provide direct information regarding electronic transitions between the valence and conduction bands [26, 27].

Figure 4 presents the UV–Vis absorption spectra of the BNC films. All samples exhibit a pronounced absorption region in the 200–300 nm range. This region corresponds to the $n \rightarrow \pi^*$ and $\pi \rightarrow \pi^*$ electronic transitions associated with the carbonyl (C = O) and conjugated double bond (C = C) groups present in the CMC and PVP chains [28–31]. The weak absorption observed in the BNC0 sample can be attributed to the limited conjugation and low electron delocalization within the polymer chains. In contrast, a noticeable increase in absorption intensity is observed in the BNC1, BNC2, and BNC3 samples containing GO and MWCNT fillers. The strong absorption band in the 200–250 nm region of GO containing systems can be assigned to $n–\pi^*$ transitions

of C = C bonds (~ 207 nm) and π–π* transitions of C = O bonds (~ 246 nm) within the GO structure [32]. Similarly, the incorporation of MWCNTs enhances charge transfer by forming efficient electron transport pathways within the polymer matrix, thereby increasing optical density [23].

The highest absorption values were obtained for the BNC3 sample. The coexistence of GO and MWCNTs strengthens π–π interactions, enhances electron delocalization, and consequently causes a slight redshift of the absorption edge toward the visible region [33, 34]. This redshift indicates a narrowing of the band-gap and an improvement in photon absorption capability. The enhanced absorption observed in BNC3 can be attributed to the synergistic effect of the large surface area of GO and the high electrical conductivity of MWCNTs, resulting in increased polarity, higher electronic excitation probability, and more efficient photon absorption [23, 25].

The optical absorption coefficient (α) is a key optical parameter used to describe the interaction of materials with light, playing a fundamental role in understanding the nature of electronic transitions, particularly in nanocomposite systems. This coefficient quantitatively defines the amount of light absorbed by a material at a specific wavelength and can be determined using the Beer–Lambert law, expressed as follows [35]:

$$\alpha = \frac{(2.303)A}{d} \quad (1)$$

where A represents the measured absorbance value and d denotes the film thickness. This parameter is particularly useful when comparing biopolymer films with varying thicknesses [36]. The absorption coefficient spectra of the BNC films are presented in Fig. 5a, showing high absorption values in the UV region. This behavior arises from the $n \rightarrow \pi^*$ and $\pi \rightarrow \pi^*$ electronic transitions associated with the carbonyl (C = O) and unsaturated C = C groups in the CMC/PVP matrix [28, 30, 37]. The incorporation of CNTs and GO enhances π–π interactions within the material, leading to increased photon absorption and a broader range of electronic transition possibilities [32, 38].

The variation of the absorption coefficient with wavelength exhibits a decreasing trend from high values in the shorter wavelength region toward the visible range. This trend reflects the characteristic optical damping mechanism within the biocomposite matrix. The absorption edge values are listed in Table 2, showing that with increasing CNT and GO content, the absorption edge shifts from 5.31 eV to 5.12 eV. This redshift is associated with band-gap narrowing and the facilitation of charge carrier transitions within the composite [39–41].

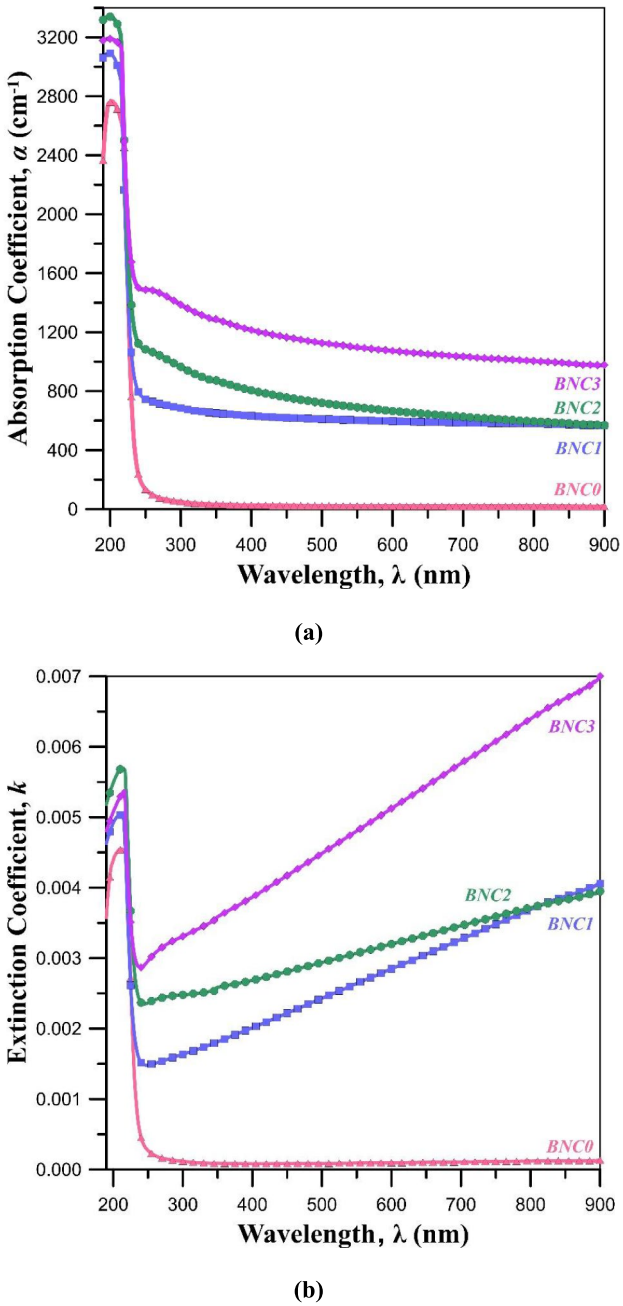

Fig. 5 **a** Absorption coefficient (α) and **b** extinction coefficient (k) spectra of the BNC films

The extinction coefficient (k), which represents the imaginary part of the complex refractive index, is a critical parameter in determining the suitability

Table 2 Absorption Edge, Urbach energy (E_u) and optical band gap energies (E_g^d and E_g^i) obtained with Tauc and ASF methods for BNC films

Bio-nano-composites	Absorption edge (eV)	Tauc method			ASF method		
		E_g^d(eV)	E_g^i(eV)	E_u (eV)	E_g^d(eV)	E_g^i(eV)	E_u (eV)
BNC0	5.31 ± 0.0070	5.45 ± 0.0141	5.13 ± 0.0014	0.17 ± 0.0014	5.44 ± 0.0063	5.11 ± 0.0035	0.17 ± 0.0007
BNC1	5.27 ± 0.0254	5.42 ± 0.0070	4.92 ± 0.0388	0.31 ± 0.0106	5.41 ± 0.0141	4.95 ± 0.0395	0.31 ± 0.0148
BNC2	5.21 ± 0.0084	5.41 ± 0.0070	4.82 ± 0.0304	0.38 ± 0.0021	5.41 ± 0.0169	4.84 ± 0.0049	0.38 ± 0.0028
BNC3	5.12 ± 0.0056	5.36 ± 0.0007	4.67 ± 0.0007	0.48 ± 0.0049	5.36 ± 0.0014	4.67 ± 0.0056	0.48 ± 0.0091

of materials for optoelectronic applications. This coefficient quantifies the fraction of electromagnetic energy lost per unit thickness due to scattering and absorption within a medium and can be calculated using the following relation [42]:

$$k = \frac{\alpha \lambda}{4\pi} \tag{2}$$

where α denotes the absorption coefficient and λ represents the photon wavelength. Figure 5b illustrates the variation of the extinction coefficient (k) of BNC films as a function of wavelength. As observed from the graph, the pure CMC/PVP (BNC0) sample exhibits a very low extinction coefficient with a sharp decrease in the 200–300 nm range. With increasing CNT-GO content (BNC1-BNC3), a noticeable rise in k values is observed. This can be attributed to enhanced photon scattering in the presence of nanofillers, leading to greater attenuation of light within the material [43].

The addition of CNTs–GO increases the charge carrier density in the nanocomposites, thereby strengthening the light–matter interaction and consequently enhancing the absorption coefficient. This results in a higher rate of electromagnetic energy loss, which manifests as an increase in the extinction coefficient [44].

At shorter wavelengths (UV region, < 350 nm), the k values are relatively high due to the elevated photon energy, which causes intense optical absorption. As the wavelength extends into the visible and near-infrared region (400–900 nm), a slight increase in k is observed, indicating that light scattering on CNTs and GO surfaces becomes the dominant effect. This behavior demonstrates that the carbon-based hybrid structure enhances photonic interactions and improves the nanocomposite's capability to dissipate optical energy.

3.4 Determination of optical band-gap energy

In semiconductor materials, the band-gap energy (E_g) is defined as the minimum energy required for an electron to transition from the valence band to the conduction band [45]. In polymeric materials, this energy gap is additionally interpreted as the difference between the highest occupied molecular orbital (HOMO) and the lowest unoccupied molecular orbital (LUMO). E_g is a critical parameter that governs both the optical performance and the electronic properties of materials. In advanced technologies, such as photovoltaic systems, light emitting diodes, lasers, photodetectors, and photocatalytic applications, the functionality of semiconductors is directly linked to their band-gap energy [46]. Several spectroscopic approaches are employed to determine the optical band-gap, including the Tauc plot, Kubelka–Munk (K–M), absorption spectrum fitting (ASF), and dielectric loss methods [45, 47–49]. Since each method is based on different assumptions, discrepancies in the measured results can arise. Therefore, a definitive consensus on the most suitable method for optical band-gap determination has not yet been established in the literature [50]. To ensure reliable evaluation of thin, semi-transparent polymer nanocomposites, multiple band-gap estimation methods were applied and selected based on their suitability for the material's optical characteristics, allowing cross-validation of the results.

3.4.1 Tauc method

The Tauc relation is one of the most widely used analytical methods for determining the optical band-gap energy (E_g) and is particularly regarded as a standard approach for amorphous and non-crystalline semiconductors [46, 51]. Originally proposed by Tauc in 1966 for estimating E_g from the optical absorption spectra of amorphous semiconductors, the method was later refined by Davis and Mott, gaining broad acceptance in the scientific literature [45]. The relationship between the absorption coefficient (α) of a material and the photon energy ($h\nu$) is expressed through the Tauc equation.

$$\alpha h\nu = B\left(h\nu - E_g\right)^m \tag{3}$$

Here, α denotes the absorption coefficient, hν represents the photon energy, B is a material dependent proportionality constant, E_g is the optical band-gap energy, and m corresponds to the type of electronic transition. The parameter m is defined as 1/2 for direct allowed transitions and 2 for indirect allowed transitions [52]. For the BNC films, the $(\alpha h\nu)^2 - h\nu$ and $(\alpha h\nu)^{1/2} - h\nu$ plots are presented in Fig. 6a and b, respectively. The direct (E_g^d) and indirect (E_g^i) optical band-gap energies were determined by extrapolating the linear regions of these plots to the hν axis. The obtained values are listed in Table 2. Similar observations have been reported for polymer-based nanocomposites, where both direct and indirect band-gap energies are estimated using the Tauc approach; however, the dominant transition type is determined based on the best linear fit of the corresponding plots. Both $(\alpha h\nu)^2$ and $(\alpha h\nu)^{1/2}$ plots exhibit reasonably linear regions, suggesting that direct and indirect transitions may coexist in the BNC films.

The Tauc method is a widely employed optical analysis approach for determining the optical band-gap of amorphous semiconductors; however, its application involves certain challenges. These include: (i) the calculation of the absorption coefficient (α) typically requires knowledge of the film thickness and may introduce uncertainty in optical analyses. In the present study, however, variations in film thickness did not lead to a significant change in the calculated E_g values, indicating that the observed band-gap behavior is primarily governed by nanofiller-induced modifications rather than thickness-related effects. (ii) The determination of the band-gap from the Tauc plot relies on selecting a linear tangent to the curve, which is inherently subjective and may lead to slight discrepancies between different researchers. (iii) Another critical aspect of the method is the determination of the exponential parameter (m), which depends on the nature of the electronic transition and remains one of the most sensitive factors in E_g estimation [35].

3.4.2 ASF method

To ensure the reliable determination of the optical band-gap, the Absorbance Spectrum Fitting (ASF) model was also employed to verify the values obtained through the graphical Tauc approach. By rearranging Eq. 3, the ASF model can be expressed as follows:

$$A = C\lambda\left(h\nu - E_g\right)^m \tag{4}$$

Here, $C = Bd/hc(2.303)$ is constant. The optical band-gap energy is obtained by extrapolating to zero the linear portion of the plot of $(A\lambda^{-1})^{m^{-1}}$ versus $h\nu$. In this way, optical band-gap energies can be determined directly from absorbance data without requiring precise knowledge of sensitive measurement parameters such as sample thickness or solution concentration.

In the present study, for the BNC films, the $(A\lambda^{-1})^2 - h\nu$ and $(A\lambda^{-1})^{1/2} - h\nu$ plots are presented in Figures S1a and b, respectively. The direct (E_g^d) and indirect (E_g^i) optical band-gap energies were determined by extrapolating the linear regions of these plots to the $h\nu$ axis. The obtained values are listed in Table 2.

3.4.3 K-M method

The Kubelka–Munk (K–M) method is a widely used semi empirical model for extracting the optical band-gap from reflectance measurements, particularly in highly scattering powder systems or multilayer thin films [53]. Developed by Paul Kubelka and Franz Munk in 1931, this approach relies on the Kubelka–Munk function, which converts measured diffuse reflectance into a pseudo absorption coefficient and is expressed as follows [54]:

$$F(R) = \frac{K}{S} = \frac{(1-R)^2}{2R} \tag{5}$$

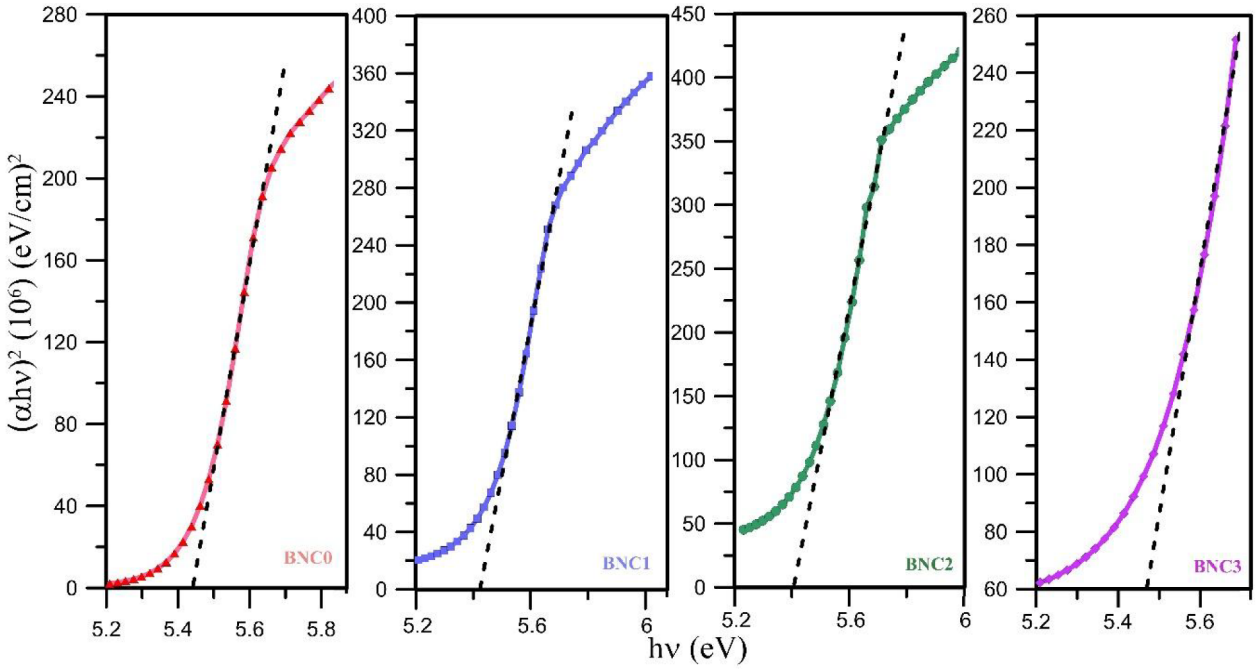

(a)

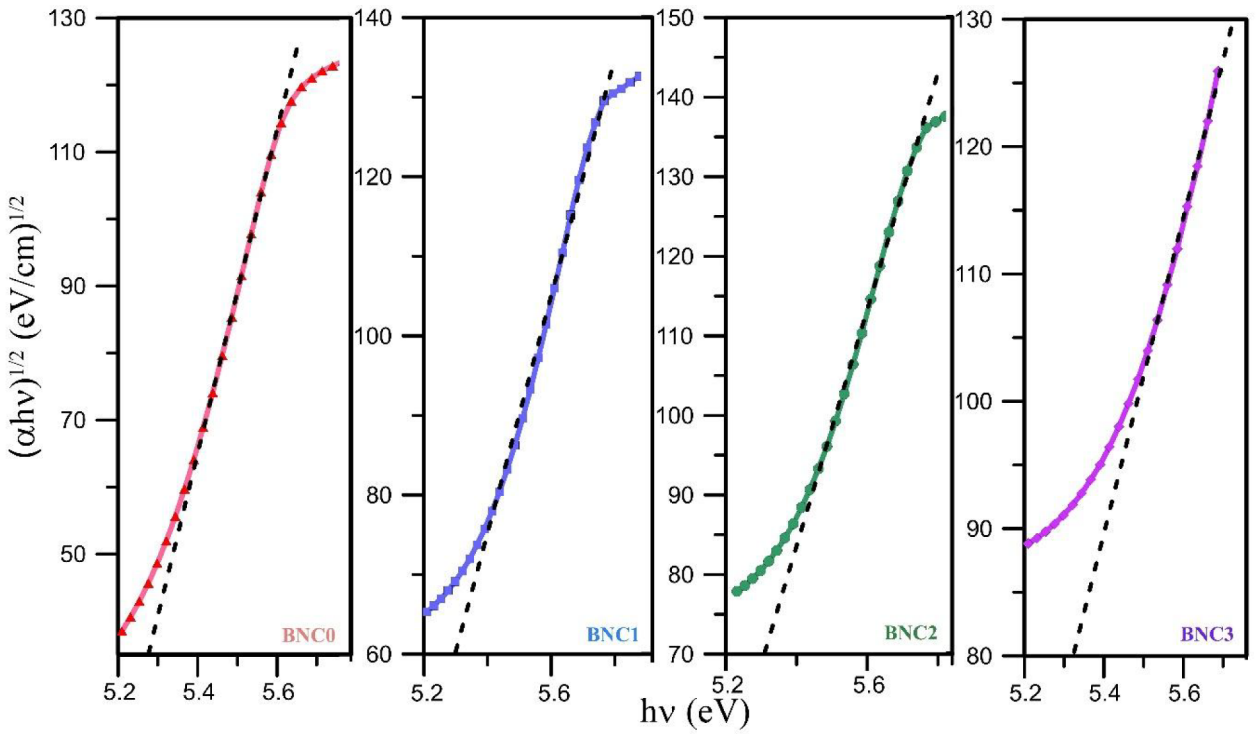

(b)

Fig. 6 **a** $(\alpha h\nu)^2$ versus $(h\nu)$ plot and **b** $(\alpha h\nu)^{1/2}$ versus $(h\nu)$ plot of BNC films

Here, the reflectance value R of an optically thick sample is used to establish the ratio K/S, which represents the absorption coefficient [53]. In this way, $F(R)$ becomes an alternative quantity to the absorption coefficient (α) used in the Tauc method, and can be expressed as:

$$F(R)h\nu = B\left(h\nu - E_g\right)^m \quad (6)$$

By plotting $(F(R)h\nu)^{1/m}$ against $h\nu$, the optical band-gap energies corresponding to both direct and indirect transitions can be determined from the point where the linear region intercepts the energy axis [53]. The Tauc curves generated using the Kubelka–Munk transformation for the BNC films, representing direct (E_g^d) and indirect (E_g^i) allowed transitions, are presented in Figures S2a and b. The calculated E_g^d and E_g^i values are summarized in Table 3.

Since this procedure relies on a graphical analysis similar to the Tauc method, sources of uncertainty such as the arbitrariness in selecting the tangent line and the ambiguity of the exponent m, which determines the type of transition, persist in this approach as well [55]. Nonetheless, the K-M model offers significant advantages for materials in which light undergoes strong scattering; under conditions of diffuse illumination, the resulting band-gap estimations have been shown to be reliable [56].

3.4.4 Estimation of E_g from dielectric loss

The strong relationship between the band structure of materials and their optical responses is well established, and the imaginary part of the dielectric function (ε_i) plays a critical role in describing electronic absorption processes arising from interactions with the electromagnetic field in an isotropic medium [57]. Since optical transitions are directly represented by the loss features in the ε_i spectrum, the optical band-gap energy can often be estimated by extrapolating the linear region of the ε_i–$h\nu$ curve to zero loss [5]. The increase in ε_i observed with rising $h\nu$ in composite materials is attributed to the formation of conductive pathways by carbon-based fillers within polymer matrices, which enhances leakage currents and consequently leads to energy dissipation. The decrease in ε_i up to the maximum absorption region, followed by a sharp rise at higher photon energies, reflects energy losses associated with polarization processes. From a quantum mechanical perspective, the main peaks of the dielectric function correspond to strong interband transitions; therefore, ε_i-based analysis can serve as a complementary method to the Tauc model for determining the band-gap [38].

The extrapolation of the linear segment of the ε_i–$h\nu$ curve for the BNC films to zero is presented in Figure S3. The extracted E_g values are listed in Table 3. It has been reported in the literature that, in polymeric systems, ε_i is directly correlated with the density of states within the forbidden band, and an increase in the density of states may lead to a reduction in the E_g value [58].

3.4.5 Evaluation of the E_g values and determination methods

For comparison, the full optical band-gap (E_g) and absorption edge values of the BNCs are presented in Fig. 7. As seen in the figure, the incorporation of carbon fillers (CFs) into the BNCs leads to a pronounced decrease in the optical band-gap energy. This trend can be attributed to the formation of localized energy states within the band structure due to the added CFs, which act as electron traps and thereby narrow the energy difference between the valence and conduction bands [59]. The increase in CF content also promotes the generation of additional charge carriers, which enhances the electrical conductivity of the material

Table 3 Refractive index (n), and optical band gap energies of the BNC films, estimated using the dielectric loss model and K-M method

Bio-nanocomposites	n (at 600 nm)	E_g from ε_i	K-M method	
			E_g^d(eV)	E_g^i(eV)
BNC0	1.75	5.31 ± 0.0021	5.31 ± 0.0056	3.77 ± 0.0014
BNC1	1.80	5.28 ± 0.0007	5.26 ± 0.0141	3.51 ± 0.0042
BNC2	1.84	5.21 ± 0.0042	5.19 ± 0.0141	3.08 ± 0.0021
BNC3	1.88	5.09 ± 0.0021	5.08 ± 0.0014	2.84 ± 0.0035

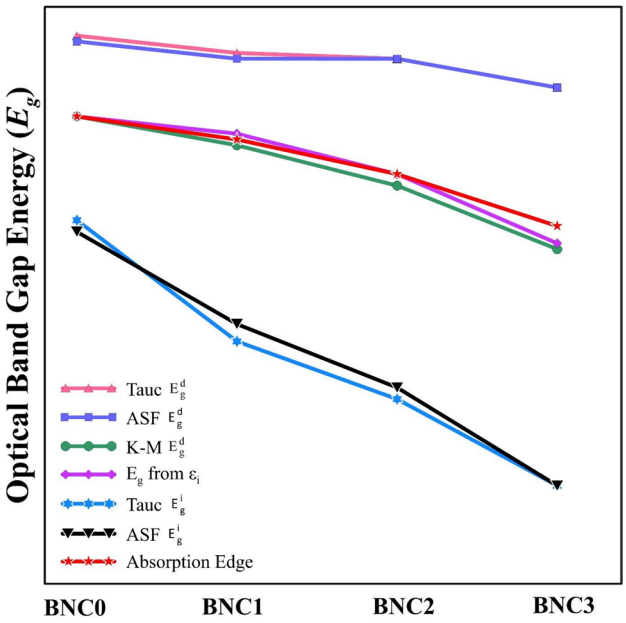

Fig. 7 Variation of the optical band gap energy values obtained from different methods for the BNC films

[42]. Furthermore, the presence of CFs increases the number of electrons capable of absorbing photons, resulting in a further reduction in E_g and an improvement in the conductivity of the BNC films [60]. This overall band-gap narrowing behavior is considered to arise from the additional localized energy levels and charge transfer complexes created by CF incorporation [35]. Such development may also be associated with the formation of effective conductive pathways within the CMC/PVP hybrid matrix, as the CFs establish interconnected network structures [61].

In addition, this behavior can be further explained in terms of charge transport mechanisms in polymer–nanofiller systems. The incorporation of GO and MWCNTs introduces defect induced localized states that facilitate charge hopping or tunneling between adjacent sites [8, 62]. Moreover, interfacial interactions between the polymer matrix and the nanofillers can generate interfacial polarization regions, which contribute to enhanced charge carrier mobility and modification of the electronic structure [7, 63]. These combined effects localized states, interfacial polarization, and percolative transport pathways collectively account for the observed reduction in the optical band-gap.

In particular, the superior optical performance observed in the GO/MWCNT hybrid system (BNC3) can be attributed to the synergistic interaction between these two nanocarbon fillers. GO, due to its oxygen-containing functional groups, introduces localized electronic states and facilitates strong interfacial interactions with the polymer matrix, while MWCNTs provide highly conductive pathways for charge transport. In the hybrid structure, GO sheets can act as electron acceptors, whereas MWCNTs function as conductive bridges, enabling efficient charge transfer across the composite. This synergistic effect enhances charge separation and suppresses carrier recombination, leading to improved optical absorption and reduced band-gap compared to single filler systems. Similar behavior has been reported in hybrid graphene–CNT systems, where interconnected conductive networks and interfacial charge transfer significantly enhance the optoelectronic properties of nanocomposites [64–66].

Figure 7 shows that the E_g^d and E_g^i values calculated using both the Tauc and ASF methods are very close to each other, indicating that the CFs are homogeneously dispersed within the CMC/PVP matrix [22]. The E_g^d values determined via the K–M method are found to be consistent with those obtained from the dielectric loss method, and the absorption edge values display similar trends across all approaches.

It should be noted that the obtained optical band-gap values ($E_g^i = 4.67 - E_g^d = 5.4$ eV) are relatively high compared to conventional semiconducting nanocomposite systems. In polymer-based nanocomposites, particularly those containing carbon nanofillers such as GO and MWCNTs, the absorption edge is largely governed by localized states, tail states, and defect-induced energy levels within the band structure. These localized states arise from structural disorder, interfacial interactions, and the heterogeneous distribution of nanofillers, leading to band tailing effects that dominate the optical transitions. Therefore, the extracted band-gap values reflect transitions involving these sub-band states rather than direct valence-to-conduction band transitions. This interpretation is further supported by the observed increase in Urbach energy (E_u), which indicates enhanced disorder and the presence of extended localized states within the forbidden gap.

The question of whether the composites exhibit allowed direct or allowed indirect transitions remains a subject of debate in the literature. Therefore, both E_g^d and E_g^i values were calculated for the BNCs in this study. In all three methods Tauc, ASF, and K–M the E_g^i

values were consistently lower than the E_g^d values, a result that has also been widely reported in previous studies [5, 25, 34, 37, 53]. Additionally, the E_g values derived from the dielectric loss method, which does not require knowledge of the transition type exponent m, were found to be close to the E_g^d values obtained using the K–M method.

3.5 Determination of urbach energy

Low crystallinity, structural disorder, and amorphous characteristics in polymer composites are known to cause the absorption coefficient to exhibit an exponential behavior near the band edge, commonly referred to as the Urbach tail [40, 41, 67]. This tail reflects the presence of localized states extending into the forbidden band-gap and is critically important for understanding the electronic transport mechanisms in the material [15]. The Urbach energy (E_u) is a quantitative measure of the width of these band tails and serves as a direct indicator of defect states and structural disorder generated after doping [41]. In amorphous composites, the dependence of the absorption coefficient on photon energy in the low photon energy region follows the exponential relation proposed by Urbach [68]:

$$\alpha = \alpha_0 \exp\left(\frac{h\nu}{E_u}\right) \tag{7}$$

where α_0 denotes a characteristic constant specific to the composite, and E_u represents the Urbach energy defining the width of the band tail created by localized energy states within the band-gap. Using Eq. (7), the E_u values were obtained from the reciprocal slopes of the linear regions of the lnα–$h\nu$ plots shown in Fig. 8a, and the extracted values are presented in Table 2.

The E_u can also be derived directly from absorbance data without requiring film thickness, instead of using the absorption coefficient. When the ASF approach is used, Eq. (7) can be rearranged as follows:

$$A = F\exp\left(\frac{hc}{E_u\lambda}\right) \tag{8}$$

where $F = (\alpha_0 d/2.303)$. In the ASF procedure, the E_u values of the BNCs were determined from the slopes of the linear regions of the ln(A)–($1/\lambda$) plots shown in Fig. 8b, using the relation $E_u = 1239.83/slope$, and the results are listed in Table 2.

As shown in Table 2, the E_u values obtained from both approaches are identical. The lowest E_u value was 0.17 eV for BNC0 (the pure CMC/PVP bionanocomposite), whereas the highest E_u value reached 0.48 eV for BNC3 (the CMC/PVP/GO/MWCNT bionanocomposite). Studies in the literature report that the incorporation of carbon-based fillers into nanocomposite matrices increases E_u while simultaneously reducing the optical band-gap energy (E_g) [69, 70]. This confirms that the disorder introduced by the filler phase promotes the formation of new localized sub-band states within the band-gap. Therefore, the increase in E_u indicates that the composite acquires a more amorphous character and exhibits a higher defect density [41].

This behavior can be further explained in terms of band tailing effects associated with structural disorder in polymer nanocomposites. The incorporation of GO and MWCNTs introduces structural imperfections and interfacial heterogeneity, leading to the formation of exponential band tails extending into the band-gap region. These band tails originate from defect states and localized energy levels induced by filler–matrix interactions. In particular, interfacial regions between the polymer chains and nanofillers act as energetically disordered zones, facilitating the formation of trap states and broadening of the absorption edge. As a result, the increase in Urbach energy reflects enhanced disorder, stronger interfacial interactions, and a higher density of localized states within the band structure.

A stronger structure–property correlation can be established by considering the relationship between nanofiller dispersion, structural disorder, and optical transitions. The SEM observations indicate that the incorporation of GO and MWCNTs leads to a heterogeneous yet well-distributed filler network within the polymer matrix. Such dispersion, although macroscopically uniform, introduces numerous interfacial regions and localized heterogeneities at the nanoscale. These interfacial regions act as sources of structural disorder and defect states, which is consistent with the observed increase in Urbach energy (E_u). The rise in E_u reflects the broadening of band tail states and the formation of localized energy levels within the band-gap. As the density of these localized states increases, optical transitions increasingly occur via these sub-band states rather than through direct band-to-band transitions. Consequently, the improved dispersion of carbon nanofillers, while enhancing interfacial interaction and network formation, also promotes

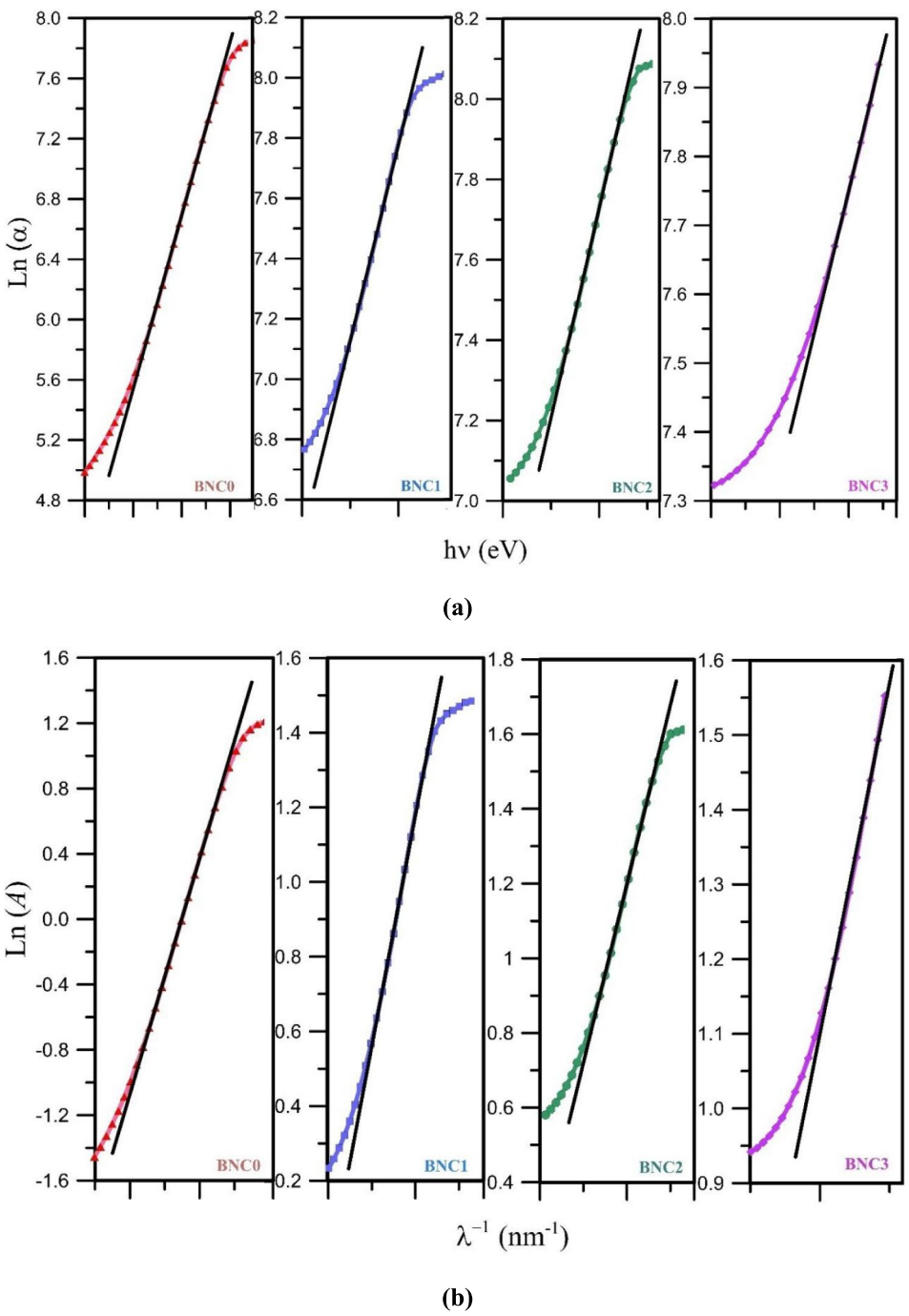

Fig. 8 **a** (ln α) versus ($h\nu$) plots **b** (ln A) versus (λ^{-1}) plots of BNC films

disorder-induced electronic states, leading to a systematic narrowing of the optically determined bandgap. This correlation demonstrates that the morphological characteristics observed in SEM are directly linked to the evolution of electronic structure and optical properties in the nanocomposite system.

3.6 Reflectance (R) and refractive index (n)

The reflectance (R) spectra of the BNC films in the 190–900 nm wavelength range are presented in Fig. 9a. All samples exhibit a distinct reflectance maximum at the onset of the UV region (≈200 nm), which indicates the materials' sensitivity to high energy photons and confirms the presence of π–π* electronic transitions

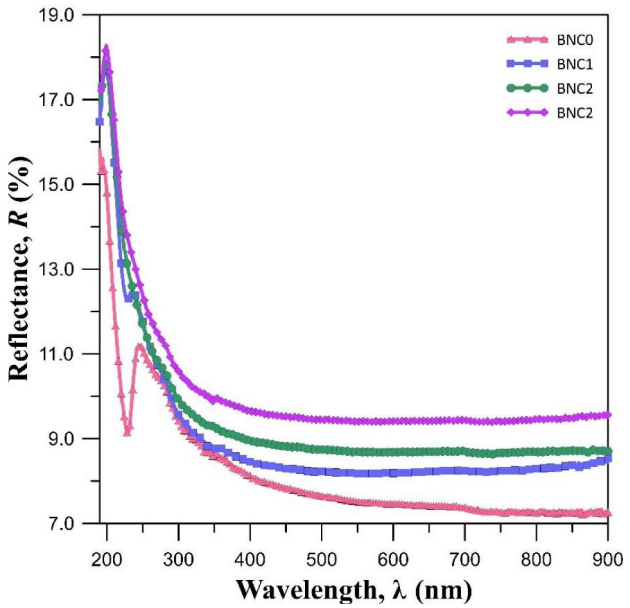

(a)

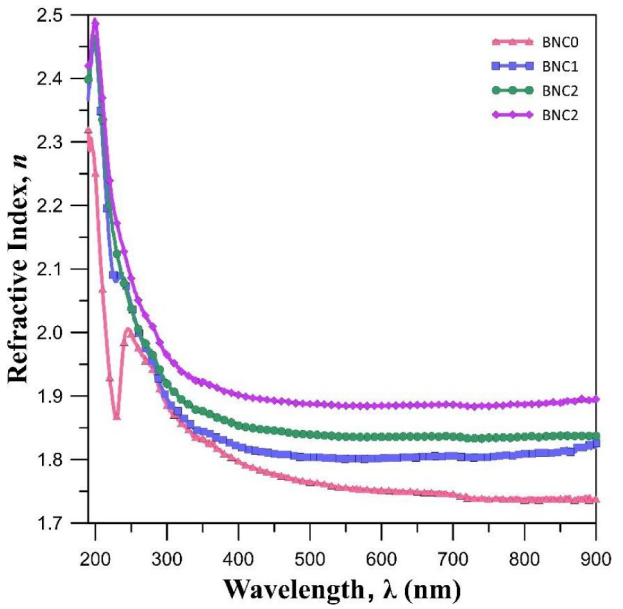

(b)

Fig. 9 **a** The reflectance (R) and **b** The refractive index (n) spectra versus wavelength (λ) BNC films

within the matrix. As the wavelength increases, the reflectance values of all BNCs decrease sharply and then transition into a more stable plateau upon entering the visible region.

The pristine CMC/PVP matrix (BNC0) displays the lowest reflectance values across the entire spectrum, whereas the incorporation of carbon-based nanofillers significantly alters the reflectance characteristics. In the GO containing BNC1 sample, an increase in reflectance is observed, which can be attributed to GO's large surface area and the delocalized π-electrons in its aromatic structure, enhancing photon–material interactions. The MWCNT-reinforced BNC2 sample exhibits even higher reflectance than BNC1, owing to the superior electron mobility and electrical conductivity of MWCNTs. The BNC3 sample, containing both GO and MWCNTs, achieves the highest reflectance values over the entire wavelength range. This enhancement is associated with the synergistic effect between GO's high surface area and MWCNTs' conductive nature, leading to increased light scattering within the composite.

Overall, the presence of carbon-based nanostructures enhances the reflectance of the composites, while a relatively stable reflectance region with minimal variation emerges in the 400–900 nm range as the wavelength increases. These findings demonstrate that the optical behavior of the BNCs is highly sensitive to both the type and concentration of the nanofillers, and that the GO/MWCNT hybrid system markedly improves the photonic properties of the material.

The refractive index (n) and extinction coefficient (k) are critical optical parameters that provide fundamental insight into the electronic band structure, atomic arrangement, and interaction of polymeric and nanocomposite materials with electromagnetic radiation [71]. These parameters play essential roles in modern optical technologies and are particularly important in the design of prisms, optical fibers, interferometric sensors, and anti reflective devices [72, 73]. The n values of the BNC films were calculated using the experimental reflectance (R) and extinction coefficient (k) data through the Fresnel equation given below [26, 74]:

$$n = \left(\frac{1+R}{1-R}\right) + \sqrt{\frac{4R}{(1-R)^2} - k^2} \tag{9}$$

The n spectra of the BNC films obtained from Eq. (9) are presented in Fig. 9b, and the n values at 600 nm are summarized in Table 3. The behavior of the n spectra in Fig. 9b closely mirrors the reflectance profiles shown in Fig. 9a. As seen in Table 3, the n of the BNC0 film is 1.75, which increases to 1.88 for BNC3. This enhancement observed in the composites containing

different fillers has been attributed to the reorganization of packing density within the matrix and the associated increase in polarizability [75, 76]. Furthermore, microstructural modifications arising from the interactions between the fillers and the host matrix enable the tuning of both n and k values, offering significant advantages for optoelectronic devices, photonic circuitry, and large scale optical applications [77].

3.7 Dielectric constants of the BNCs

The complex dielectric constant (ε) is one of the fundamental optical parameters describing the interaction of a material with electromagnetic waves, providing detailed insight into the mechanisms of energy storage and energy dissipation under an applied electromagnetic field [35]. This quantity comprises two components: the real part (ε_r, dielectric constant) and the imaginary part (ε_i, dielectric loss), which represent the material's ability to store electric energy and the attenuation of electromagnetic waves within the medium, respectively. The values of ε_r and ε_i are defined through their relationships with the refractive index (n) and the extinction coefficient (k), as given by the following expressions [78, 79].

$$\varepsilon = \varepsilon_r + i\varepsilon_i \tag{10}$$

$$\varepsilon_r = n^2 - k^2 \tag{11}$$

$$\varepsilon_i = 2nk \tag{12}$$

Using Eqs. (11) and (12), ε_r and ε_i were calculated for the BNC films, and their wavelength dependent variations are presented in Fig. 10a and b, respectively. As shown in the figures, the incorporation of carbon-based fillers into the CMC/PVP hybrid matrix leads to a pronounced increase in both ε_r and ε_i. This enhancement is primarily attributed to the formation of dense polarization centers within the polymer matrix, an increase in charge carrier concentration, and the introduction of localized energy states within the band-gap. These effects collectively strengthen dipole polarization at the matrix–filler interface [62, 80].

The rise observed in ε_r in Fig. 10a, particularly within the 190–450 nm range, indicates an enhanced ability of the material to store electric energy under an applied field. Meanwhile, the increase in ε_i presented in Fig. 10b reflects intensified absorption of light and stronger electromagnetic energy loss within the BNC.

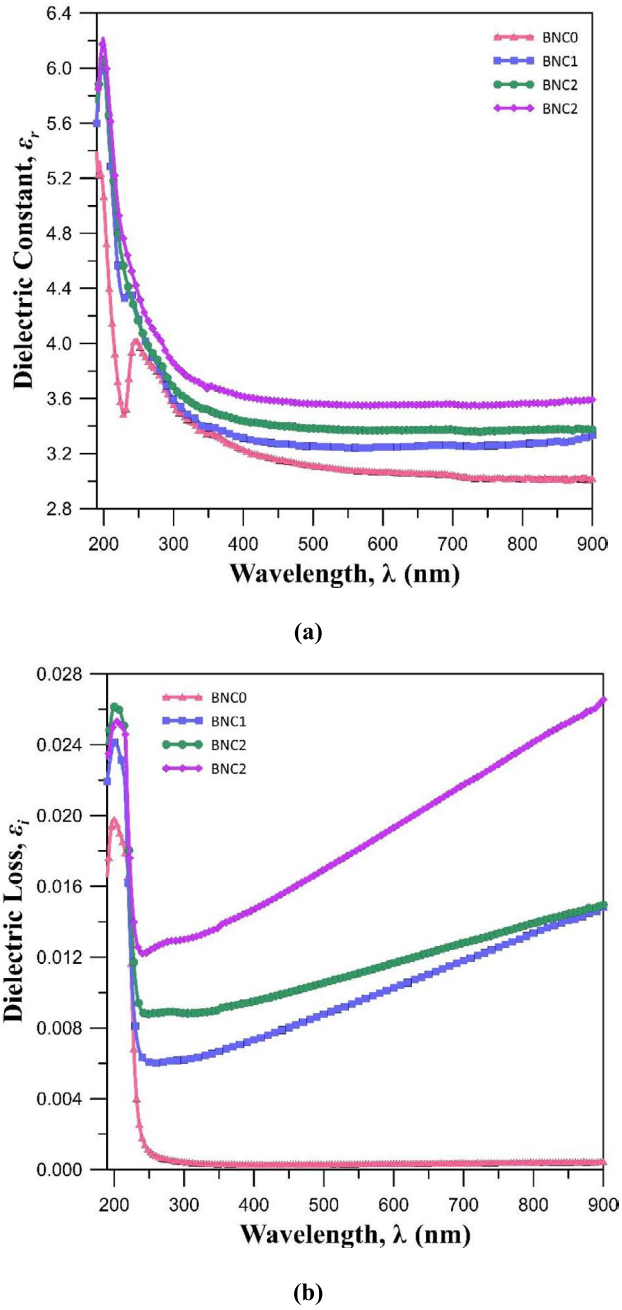

Fig. 10 **a** The dielectric constant (ε) and **b** dielectric loss (ε) spectra versus wavelength (λ) for BNC films

This behavior is directly associated with the contribution of dispersed carbon nanostructures to optical transitions and their promotion of free-charge carrier mobility.

Overall, these findings demonstrate that carbon-based filler–reinforced BNCs not only exhibit improved optical performance but also possess high

polarization capability, enhanced energy storage characteristics, and strong electromagnetic absorption properties. These features highlight their potential for applications in supercapacitor electrodes, dielectric resonators, and broadband energy storage technologies [62, 81]. Therefore, tuning the filler loading and exploring different types of carbon nanomaterials represent critical parameters in the design of advanced functional polymer nanocomposites.

4 Conclusions

In this work, the optical, dielectric, and structural properties of CMC/PVP based bionanocomposites reinforced with GO, MWCNT, and their hybrid combination were systematically investigated using multiple optical analysis approaches. The results clearly demonstrate that the incorporation of carbon-based nanofillers leads to a consistent reduction in optical band-gap (E_g) and a simultaneous increase in Urbach energy (E_u), indicating enhanced structural disorder and the formation of localized states within the band structure. These changes were accompanied by increases in absorption coefficient, refractive index, extinction coefficient, and dielectric parameters, reflecting enhanced light–matter interaction and charge carrier density in the nanocomposite system.

A key outcome of this work is the comparative evaluation of four widely used band-gap determination methods (Tauc, ASF, Kubelka–Munk, and dielectric loss) applied to the same material system. The results reveal that while all methods capture the general trend of band-gap narrowing, noticeable differences arise depending on method-specific assumptions, particularly regarding film thickness dependence and transition type selection. In this context, the ASF and dielectric loss approaches provide practical advantages for thin film systems where thickness-related uncertainties may affect conventional Tauc analysis.

Furthermore, the hybrid GO/MWCNT system exhibited the most pronounced changes in optical and dielectric properties, which can be attributed to enhanced interfacial interactions and improved charge transfer pathways within the polymer matrix.

Overall, the study provides a systematic framework for evaluating band-gap determination methods in polymer-based nanocomposites while demonstrating how carbon nanofillers influence optical transitions and disorder-related states. These findings contribute to a better understanding of method-dependent band-gap analysis and structure–property relationships in carbon-reinforced biopolymer systems.

Author Contributions

All authors contributed to the study conception and design. Material preparation, data collection and analysis were performed by Ömer Bahadır Mergen and Ertan Arda. The first draft of the manuscript was written by Ömer Bahadır Mergen and all authors commented on previous versions of the manuscript. All authors read and approved the final manuscript.

Funding

Open access funding provided by the Scientific and Technological Research Council of Türkiye (TÜBİTAK). The authors declare that no funds, grants, or other support were received during the preparation of this manuscript.

Data availability

The datasets generated during and/or analysed during the current study are available from the corresponding author on reasonable request.

Declarations

Competing interests The authors declare no competing interests.

Supplementary Information The online version contains supplementary material available at https://doi.org/10.1007/s10854-026-17312-x.

Open Access This article is licensed under a Creative Commons Attribution 4.0 International License, which permits use, sharing, adaptation, distribution and reproduction in any medium or format, as long as you give appropriate credit to the original author(s)

and the source, provide a link to the Creative Commons licence, and indicate if changes were made. The images or other third party material in this article are included in the article's Creative Commons licence, unless indicated otherwise in a credit line to the material. If material is not included in the article's Creative Commons licence and your intended use is not permitted by statutory regulation or exceeds the permitted use, you will need to obtain permission directly from the copyright holder. To view a copy of this licence, visit http://creativecommons.org/licenses/by/4.0/.

References

1. M.J. Tommalieh, N.S. Awwad, H.A. Ibrahium, A.A. Menazea, J. Mol. Struct. (2020). https://doi.org/10.1016/j.molstruc.2020.128814
2. N. Manjushree, V.L. Yashaswini, R. Kavya, M.A. Sangamesha, U. GopalakrishnaPanicker, K.M. Gowda, S.S. Revankar, P.R. Vanga, J. Thomas, B.M. Sachith, M.E. Thomas, M. Norek, S. Thomas, M.B.S. Madhukar, J. Mol. Struct. (2025). https://doi.org/10.1016/j.molstruc.2024.140780
3. A.I. Al-Sulami, A.B. Alruqi, N. Algethami, F.M.H. AlSulami, R.H. Aldahiri, A.A. Al-Ghamdi, A. Rajeh, Mater. Chem. Phys. (2024). https://doi.org/10.1016/j.matchemphys.2024.128971
4. M. Sadiq, M.A. Khan, M.M.H. Raza, S.M. Aalam, M. Zulfequar, J. Ali, ACS Omega (2022). https://doi.org/10.1021/acsomega.2c04933
5. I.M. Garnica-Palafox, A.M. Velázquez-Benítez, F.M. Sánchez-Arévalo, N. Qureshi, Opt. Mater. (2025). https://doi.org/10.1016/j.optmat.2025.116686
6. S.A. Dhanaraj, J. Mater. Sci. Mater. Electron. (2018). https://doi.org/10.1007/s10854-018-8658-3
7. Ö.B. Mergen, E. Arda, Mater. Res. Express (2026). https://doi.org/10.1088/2053-1591/ae3a46
8. A. Atta, E. Abdeltwab, H. Negm, N. Al-Harbi, M. Rabia, M.M. Abdelhamied, J. Inorg. Organomet. Polym. (2023). https://doi.org/10.1007/s10904-023-02643-7
9. A.M. Pandele, A.M. Holban, S.S. Avramescu, D.G.D. Petrescu, C.S. Tîlmaciu, M.R. Chiriţă, Compos Part B-Eng. (2017). https://doi.org/10.1016/j.compositesb.2017.06.010
10. A. Maity, Results Chem. (2025). https://doi.org/10.1016/j.rechem.2025.102877
11. T.C. Mokhena, M.J. Mochane, A. Mtibe, S. Sigonya, B. Ntsendwana, E.G. Masibi, L. Sikhwivhilu, T.S. Motsoeneng, Cellulose (2024). https://doi.org/10.1007/s10570-024-06055-9
12. M.I. Mohammed, H.Y. Zahran, S.H. Zyoud, M. Shahwan, C. Aydin, I.S. Yahia, D. Abdelhameed, J. Polym. Res. (2025). https://doi.org/10.1007/s10965-024-04219-6
13. W.-Y. Sun, W.-H. Geng, P.-F. Qian, T.-L. Wang, L.-C. Jing, J.-Y. Feng, Y.-H. Wang, Y.-X. Wang, H.-L. Zhou, H.Z. Geng, ACS Appl Polym Mater. (2025). https://doi.org/10.1021/acsapm.5c00373
14. A.Y. Yassin, M. Abdel-Raouf, E.M. Abdelrazek, M.A. Morsi, A.M. Abdelghany, J Mater Res Technol. (2019). https://doi.org/10.1016/j.jmrt.2018.08.005
15. Y. Feng, S. Lin, S. Huang, S. Shrestha, G. Conibeer, J. Appl. Phys. (2015). https://doi.org/10.1063/1.4916090
16. S. Landi Jr., I.R. Segundo, E. Freitas, M. Vasilevskiy, J. Carneiro, C.J. Tavares, Solid State Commun. (2022). https://doi.org/10.1016/j.ssc.2021.114573
17. P.V.B. Prabhuswamy, N.K. Swamy, M.B. Sangameshwar, B.K.S. Prakash, K. Rajanna, M. Basavaraju, S.M. Ankanathappa, Polymer (2025). https://doi.org/10.1016/j.polymer.2025.129137
18. M. Cui, Z. Shao, D. Lu, Macromol. Res. (2019). https://doi.org/10.1007/s13233-019-7054-z
19. M.A. Morsi, R.A. Pashameah, K. Sharma, E. Alzahrani, M.O. Farea, A.A. Al-Muntaser, J. Polym. Environ. (2022). https://doi.org/10.1007/s10924-022-02656-2
20. R.M. Ahmed, Int. J. Photoenergy (2009). https://doi.org/10.1155/2009/150389
21. S.A. Sbeih, A.M. Zihlif, J. Phys. D Appl. Phys. (2009). https://doi.org/10.1088/0022-3727/42/14/145405
22. F.M. Ali, J. Mol. Struct. (2019). https://doi.org/10.1016/j.molstruc.2019.04.014
23. C.P. Charan, R.J. Sengwa, J. Polym. Res. (2025). https://doi.org/10.1007/s10965-025-04649-w
24. F. Yakuphanoglu, M. Arslan, Opt. Mater. (2004). https://doi.org/10.1016/j.optmat.2004.01.017
25. A.T. Mosleh, H.Y. Zahran, I.S. Yahia, E.A. Kamoun, M. Abdel-Aty, M. Alfiras, M.H. Ahmed, S. Alkhazaleh, M.I. Mohammed, M.S.A. Hussien, Indian J. Phys. (2025). https://doi.org/10.1007/s12648-025-03736-4
26. O.G. Abdullah, S.B. Aziz, M.A. Rasheed, J. Mater. Sci. Mater. Electron. (2017). https://doi.org/10.1007/s10854-016-6086-9
27. O.G. Abdullah, R.R. Hanna, Y.A.K. Salman, J. Mater. Sci. Mater. Electron. (2017). https://doi.org/10.1007/s10854-017-6796-7
28. S.A. Al Hashedi, A.M. Abd El-latif, A.A. Al-Muntaser, N.S. Al-Zoreky, K.M.A. Ramadan, A.Q. Alosabi, Int. J. Biol. Macromol. (2025). https://doi.org/10.1016/j.ijbiomac.2025.141840

29. M.M. Atta, E. Aldosari, H.M.H. Zakaly, Q. Zhang, J. Inorg. Organomet. Polym. Mater. (2025). https://doi.org/10.1007/s10904-025-03760-1
30. S.R. Al-Mhyawi, A.I. Al-Sulami, F.M.H. Al-Sulami, R.H. Aldahiri, M.M. Alsabban, F. J Sci Adv Mater Devices. (2025). https://doi.org/10.1016/j.jsamd.2025.100920
31. M.J. Al-Issawe, M.A. Habeeb, A.R. Abdulridha, J. Mater. Emerg Mater. (2025). https://doi.org/10.1007/s42247-025-01204-7
32. R. Badry, N.M. Sabry, M.A. Ibrahim, Sci. Rep. (2024). https://doi.org/10.1038/s41598-024-81365-3
33. A.A. Alhazime, Inorg. Chem. Commun. (2025). https://doi.org/10.1016/j.inoche.2025.115664
34. A.A. Al-Muntaser, R.A. Althobiti, M.A. Morsi, H.A. Alsalmah, A.E. Tarabiah, E. Alzahrani, A.N. Al-Hakimi, E.M. Abdallah, Int. J. Biol. Macromol. (2024). https://doi.org/10.1016/j.ijbiomac.2023.127894
35. Ö.B. Mergen, E. Arda, J. Mater. Sci. Mater. Electron. (2023). https://doi.org/10.1007/s10854-023-11152-9
36. N.A.A. Anas, Y.W. Fen, N.A.S. Omar, N.S.M. Ramdzan, W.M.E.M.M. Daniyal, S. Saleviter, A.A. Zainudin, Opt. Laser Technol. (2019). https://doi.org/10.1016/j.optlastec.2019.105724
37. M.O. Alziyadi, A. Alruwaili, A.M.B. Said, M.S. Shalaby, Appl. Phys. A (2025). https://doi.org/10.1007/s00339-024-08195-y
38. S.B. Aziz, O.G. Abdullah, M.A. Rasheed, J. Appl. Polym. Sci. (2017). https://doi.org/10.1002/app.44847
39. I.S. Yahia, M.I. Mohammed, J. Mater. Sci. Mater. Electron. (2018). https://doi.org/10.1007/s10854-018-8869-7
40. S.B. Aziz, J. Electron. Mater. (2016). https://doi.org/10.1007/s11664-015-4191-9
41. S.B. Aziz, O.G. Abdullah, A.M. Hussein, R.T. Abdulwahid, M.A. Rasheed, H.M. Ahmed, J. Mater. Sci. Mater. Electron. (2017). https://doi.org/10.1007/s10854-017-6437-1
42. Ö.B. Mergen, J. Compos. Mater. (2021). https://doi.org/10.1177/00219983211037050
43. T.E. Somesh, M.Q.A. Al-Gunaid, B.S. Madhukar, Siddaramaiah. J. Mater. Sci. Mater. Electron. (2019). https://doi.org/10.1007/s10854-018-0226-3
44. D.A. Nasrallah, M.A. Ibrahim, J. Polym. Res. (2022). https://doi.org/10.1007/s10965-022-02943-5
45. P. Makuła, M. Pacia, W. Macyk, J. Phys. Chem. Lett. (2018). https://doi.org/10.1021/acs.jpclett.8b02892
46. L. Jarosiński, J. Pawlak, S.K.J. Al-Ani, Opt. Mater. (2019). https://doi.org/10.1016/j.optmat.2018.12.041
47. K. Baishya, J.S. Ray, P. Dutta, P.P. Das, S.K. Das, Appl. Phys. A (2018). https://doi.org/10.1007/s00339-018-2097-0
48. Y.S. Rammah, A.A. Ali, R. El-Mallawany, A.M. Abdelghany, J. Mol. Struct. (2019). https://doi.org/10.1016/j.molstruc.2018.07.071
49. Ł Haryński, A. Olejnik, K. Grochowska, K. Siuzdak, Opt. Mater. (2022). https://doi.org/10.1016/j.optmat.2022.112205
50. N. Sangiorgi, L. Aversa, R. Tatti, R. Verucchi, A. Sanson, Opt. Mater. (2017). https://doi.org/10.1016/j.optmat.2016.11.014
51. M.E. Sánchez-Vergara, J.C. Alonso-Huitron, A. Rodriguez-Gómez, J.N. Reider-Burstin, Molecules (2012). https://doi.org/10.3390/molecules170910000
52. K. Rajanna, B.S. Madhukar, S.D. Babu, Y.V. Lokesh, K.S. Ningappa, J. Lumin. (2025). https://doi.org/10.1016/j.jlumin.2024.120977
53. Ö.B. Mergen, E. Arda, Opt. Mater. (2023). https://doi.org/10.1016/j.optmat.2023.113823
54. P. Kubelka, F. Munk, Z. Techn Physik. (1931). https://www.graphics.cornell.edu/~westin/pubs/kubelka.pdf
55. R. López, R. Gómez, J. Sol-Gel Sci. Technol. (2012). https://doi.org/10.1007/s10971-011-2582-9
56. A. Sáenz-Trevizo, P. Amézaga-Madrid, P. Pizá-Ruiz, W. Antúnez-Flores, M. Miki-Yoshida, Mater. Res. (2016). https://doi.org/10.1590/1980-5373-MR-2015-0612
57. D.S. Muhammad, D.M. Aziz, S.B. Aziz, RSC Adv. (2024). https://doi.org/10.1039/d4ra04228j
58. D.A. Tahir, Alex. Eng J. (2022). https://doi.org/10.1016/j.aej.2021.06.088
59. G. Soni, N. Gouttam, P. Soni, Mater. Today Proc. (2020). https://doi.org/10.1016/j.matpr.2020.04.027
60. Ö.B. Mergen, E. Arda, Synth. Met. (2020). https://doi.org/10.1016/j.synthmet.2020.116539
61. F. Usman, J.O. Dennis, K.C. Seong, A.Y. Ahmed, F. Meriaudeau, O.B. Ayodele, A.R. Tobi, A.A.S. Rabih, A. Yar, Res. Phys. (2019). https://doi.org/10.1016/j.rinp.2019.102690
62. A. Badawi, S.S. Alharthi, Appl. Phys. A (2023). https://doi.org/10.1007/s00339-023-06640-y
63. Z.A. Raza, R. Waseem, M. Aslam, S.A.H. Bukhari, S.M.A. Zaidi, Colloid Polym. Sci. (2025). https://doi.org/10.1007/s00396-025-05452-1
64. M. Goumri, B. Lucas, B. Ratier, M. Baitoul, Opt. Mater. (2016). https://doi.org/10.1016/j.optmat.2016.07.010
65. A. Aykaç, H. Gergeroglu, B. Beşli, E.Ö. Akkaş, A. Yavaş, S. Güler, F. Güneş, M. Erol, Nanoscale Res. Lett. (2021). https://doi.org/10.1186/s11671-021-03519-w
66. J. Wu, H. Lin, D.J. Moss, K.P. Loh, B. Jia, Nat. Rev. Chem. (2023). https://doi.org/10.1038/s41570-022-00458-7

67. A.S. Hassanien, A.A. Akl, Superlattices Microstruct. (2016). https://doi.org/10.1016/j.spmi.2015.10.044
68. F. Urbach, Phys. Rev. (1953). https://doi.org/10.1103/PhysRev.92.1324
69. M. El Achaby, N. El Miri, A. Snik, M. Zahouily, K. Abdelouahdi, A. Fihri, A. Barakat, A. Solhy, J. Appl. Polym. Sci. (2016). https://doi.org/10.1002/app.42356
70. H.M. Alghamdi, A. Rajeh, J. Inorg. Organomet. Polym. (2022). https://doi.org/10.1007/s10904-022-02322-z
71. C.O. Saeed, A.A. Aziz, Opt. Mater. (2022). https://doi.org/10.1016/j.optmat.2022.112502
72. I.M. Radaf, Appl. Phys. A (2019). https://doi.org/10.1007/s00339-019-3114-7
73. D.M. Aziz, S.J. Mohammed, P.A. Mohammed, S. Al-Zangana, S.B. Aziz, D.S. Muhammad, R.T. Abdulwahid, A.H.A. Darwesh, S.A. Hussein, Spectrochim. Acta A Mol Biomol. Spectrosc. (2024). https://doi.org/10.1016/j.saa.2024.125142
74. G. Patel, M.B. Sureshkumar, P. Patel, Adv. Mater. Res. (2012). https://doi.org/10.4028/www.scientific.net/AMR.383-390.3249
75. A.M. El-Naggar, Z.K. Heiba, A.M. Kamal, Y. Altowairqi, M.B. Mohamed, O.H. Abd-Elkader, A.A. Alhazime, Opt. Mater. (2022). https://doi.org/10.1016/j.optmat.2022.112923
76. A.M. El Sayed, A.D.M. Mohamad, J. Polym. Res. (2018). https://doi.org/10.1007/s10965-018-1571-x
77. A.M. Hussein, E.M.A. Dannoun, S.B. Aziz, M.A. Brza, R.T. Abdulwahid, S.A. Hussen, S. Rostam, D.M.T. Mustafa, D.S. Muhammad, Polymers (2020). https://doi.org/10.3390/polym12102320
78. M. Aftab, M.Z. Butt, D. Ali, F. Bashir, T.M. Khan, Opt. Mater. (2021). https://doi.org/10.1016/j.optmat.2021.111369
79. K.K. Ahmed, S.B. Aziz, R.T. Abdulwahid, S.A. Hussen, M.A. Brza, Opt. Mater. (2022). https://doi.org/10.1016/j.optmat.2022.113112
80. F. Usman, J.O. Dennis, A.Y. Ahmed, K.C. Seong, Y.W. Fen, A.R. Sadrolhosseini, F. Meriaudeau, P. Kumar, O.B. Ayodele, J. Mater. Res. Technol. (2020). https://doi.org/10.1016/j.jmrt.2019.11.072
81. A.M. El-Naggar, Z.K. Heiba, A.M. Kamal, O.H. Abd-Elkader, M. Abdellatief, M.A. Mohamed, J. Vinyl Addit. Technol. (2024). https://doi.org/10.1002/vnl.22028

Publisher's Note Springer Nature remains neutral with regard to jurisdictional claims in published maps and institutional affiliations.